Applied Catalysis B: Environmental 227 (2018) 13–23

Contents lists available at ScienceDirect

Applied Catalysis B: Environmental

journal homepage: www.elsevier.com/locate/apcatb

Eco-friendly controllable synthesis of highly dispersed ZIF-8 embedded in porous Al_2O_3 and its hydrogenation properties after encapsulating Pt nanoparticles

Xiaoyun Song[a], Qingxin Guan[a,*], Zitao Cheng[a], Wei Li[a,b,*]

[a] *College of Chemistry, State Key Laboratory of Elemento-Organic Chemistry, Key Laboratory of Advanced Energy Materials Chemistry (Ministry of Education), Nankai University, Tianjin 300071, China*

[b] *Collaborative Innovation Center of Chemical Science and Engineering (Tianjin), Nankai University, Tianjin 300071, China*

ARTICLE INFO

Keywords:
Solid state method
Metal organic framework
Composite
Alumina
Hydrogenation

ABSTRACT

In this paper, a new strategy was proposed to synthesize a novel composite of highly dispersed ZIF-8 embedded in porous Al_2O_3 by a solvent-free method. This is a very simple, efficient, and eco-friendly method, in which ZnO/Al_2O_3 was used as a precursor, and dimethyl imidazole was used as an organic ligand. Meso- and microporous composite of ZIF-8@Al_2O_3 was synthesized arising from the crystal growth of ZIF-8 derived from ZnO nanoparticles. Characterization results reveal that the distribution of micropores and mesopores can be controlled by simply adjusting the amount of zinc salt supported on Al_2O_3. The value of this composite is that it can simultaneously exert the advantages of ZIF-8 and Al_2O_3 support, which can significantly decrease the particle size of ZIF-8 and improve its utilization efficiency. The micropores of ZIF-8 can increase the dispersion of Pt nanoparticles, at the same time, the functional groups on the surface of Al_2O_3 can improve the selectivity of the product. Furthermore, this kind of composite material can be extended by replacing the support. Finally, the results of the activity tests showed that the obtained Pt/ZIF-8@Al_2O_3 catalyst exhibits high activity and selectivity in hydrodearomatization (HDA) and hydrodeoxygenation (HDO) reactions.

1. Introduction

Metal organic frameworks (MOFs) as a novel class of microporous materials, have been extensively studied because of their crystalline ordered networks and high surface area. MOFs have great potential applications in gas storage and separation, drug delivery, and especially in catalysis [1–5]. For more applications, lots of efforts have been focused on synthesizing MOF-based composites to enhance electrical [6–8], adsorption [9] and thermal properties [10–13]. For examples, Zhang et al. reported a hybrid material with enhanced electrocatalytic ability through confining a Cu-based MOF in macroporous carbon [14]. Recently, Pourebrahimi et al. also have synthesized MIL-101(Cr)/GNP composite by embedding graphene nanoplates into MIL-101 pores, and the composite showed an enhanced CO_2 adsorption capacity. [15] These works all have expanded ways for application or enhanced properties of MOFs.

In recent years, applying MOFs on heterogeneous catalysis has received particular interests not only because it possesses a high area surface, but it also opens up a new opportunity in green catalysis [16–22]. However, narrow pores of MOFs limited the diffusion and passing through of large molecules, which makes it cannot compete with mesoporous materials for many reactions. Hence, meso-microporous composite materials based on composting MOFs with inorganic mesoporous materials have been reported to circumvent this limitation [23,24]. Gorka et al. and coworkers reported an one-pot microwave hydrothermal method for synthesis of MOF-boehmite and silica composites using triblock-copolymer [25]. Furtado et al. reported a composite material composed of an inorganic silica modified with CuBTC [26]. Recently, a modulated formation of MOF-5 by oriented growth over SBA-15 was reported by Karimi et al., and this research gives a new strategy for designing heterogeneous catalyst based on MOFs [27]. Although above composite materials indeed offered better properties compared to the pristine MOFs, but most approaches required prefunctionalization of the inorganic matrix to attract a growth of MOFs crystals, which makes the preparation more complicated. Besides, there are some impurities may exist in the hybrid composite [15], and it is hard to control the ratio of two components [25].Therefore, to develop a simple, efficient, and eco-friendly strategy for synthesizing MOFs

* Corresponding authors at: College of Chemistry, State Key Laboratory of Elemento-Organic Chemistry, Key Laboratory of Advanced Energy Materials Chemistry (Ministry of Education), Nankai University, Tianjin 300071, China.

E-mail addresses: qingxinguan@nankai.edu.cn (Q. Guan), weili@nankai.edu.cn (W. Li).

https://doi.org/10.1016/j.apcatb.2018.01.022
Received 20 October 2017; Received in revised form 27 December 2017; Accepted 10 January 2018
Available online 10 January 2018
0926-3373/

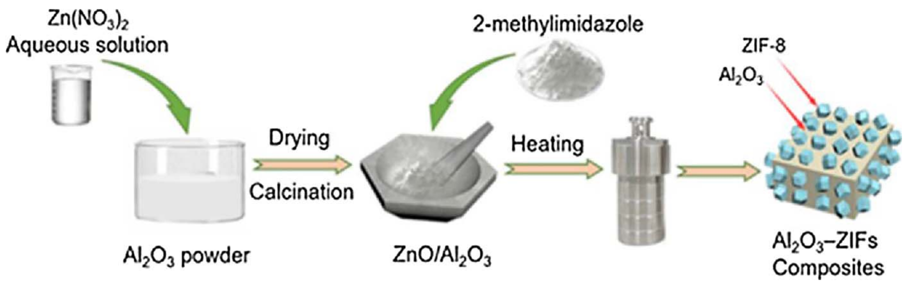

Fig. 1. Synthetic scheme of ZIF-8@Al_2O_3 composites.

composites with controllable meso- and microporosity, proper acidity, and surface area is still a great challenge.

As is well known, ZIF-8 is a famous ZIF compounds because of its relatively high thermal stability, high porosity, and large surface area, which has shown great potential in various research and industrial areas, especially in hydrogenation catalysis [28–31]. Benefit from stability and inherent acidity [32–35], many inorganic materials have been widely used as catalyst supports. Aiming at combining high surface area of ZIF-8 with proper acidity of inorganic support materials, we describe herein a controllable synthetic process of highly dispersed ZIF-8 embedded in porous Al_2O_3 by a solvent-free method. Comparing with an extensive fabrication process involving wet-chemistry-based crystallization and separation, this method is highly efficient, controllable, and environment friendly as well as applicable for scale-up production and device fabrication. To our knowledge, this is the first report of introducing solid state method [36] to fabricate ZIF-8 based composite.

In this paper, we proposed a new strategy to synthesize the composite of highly dispersed ZIF-8 embedded in porous Al_2O_3 by a solvent-free method. As illustrated in Fig. 1, this procedure is a universal and high-yield strategy for porous materials compositing with ZIF-8, and the component can be controlled by simply adjusting the impregnation amount of zinc salt. A series of ZIF-8@Al_2O_3 composites with different amounts of ZIF-8 were synthesized. The morphology, component, texture, and acid property of composites were all carefully characterized and analysed. Additionally, Pt/ZIF-8@Al_2O_3 catalyst was synthesized and tested using hydrogenation reaction, which exhibits high activity and selectivity in HDA and HDO reactions.

2. Experimental

Al_2O_3 support was purchased from Tianjin Chemist Scientific Ltd. China and calcined at 600 °C for 2 h to transform into γ-Al_2O_3 phase before use. All other materials and reagents used in this work are also commercially available and were used as received without further purification.

2.1. Synthesis of composites and catalysts

Firstly, Bulk ZIF-8 was synthesized by a solid state method. ZnO powder with a diversity of morphologies were successfully prepared with the addition of different surfactants by a simple low-temperature liquid-phase method. The synthesized process of bulk ZIF-8 was according to previously reported studies [36,37], 2-methylimidazole was mixed with the synthesized ZnO powder at a molar ratio of 2.2: 1 (2-methylimidazole: ZnO), then the mixture was grinded in a mortar and sealed in an autoclave, followed by heating at 180 °C for 18 h. Finally, the product was obtained as a white powder and washed three times with deionized water, and dried in a vacuum oven at 120 °C for 4 h.

ZIF-8@Al_2O_3 was also prepared using a solvent-free solid state method. The procedure was illustrated in Fig. 1. Firstly, $Zn(NO_3)_2/Al_2O_3$ was prepared from Al_2O_3 by incipient wetness impregnation of zinc nitrate hexahydrate with different loading. Then ZnO/Al_2O_3 was obtained after calcined at 350 °C for 2 h. Subsequently, the supported oxide precursor was mixed with 2-methylimidazole at a molar ratio of 5: 1 (2-methylimidazole: ZnO). Then the mixture was grinded in a mortar and sealed in an autoclave, followed by heating at 180 °C for 18 h. Finally, the product was obtained as a white powder and was washed three times with deionized water, and dry in a vacuum oven at 120 °C for 4 h.

0.7 wt% Pt/ZIF-8@Al_2O_3 catalyst was synthesized by incipient wetness impregnation method. Because ZIF-8 is hydrophobic (test result is shown in Fig. S1) and low acid-resistant, acetone was chosen as solvent in this process. In a typical process, acetylacetonate platinum was dissolved in acetone and then the solution was impregnated into ZIF-8@Al_2O_3 support. The wet sample was dried at 80 °C for 6 h, and then reduced at 350 °C for 2 h in a flow H_2 atmosphere (50 mL/min) to obtain supported Pt nanoparticles. The reduced Pt/ZIF-8@Al_2O_3 catalysts were all passivated in a N_2 atmosphere at 40 °C for 3 h, before being exposed to air. For comparison, Pt/Al_2O_3 and Pt/ZIF-8 catalysts were also synthesized using the same impregnation method as above. In this paper, the Pt loading of all catalysts was 0.7 wt%.

2.2. Characterizations

Powder X-ray diffraction (XRD) patterns of samples were recorded on Bruker D8 focus diffractometer, with Cu Kα radiation at 40 kV and 40 mA. Transmission electron microscopy (TEM) images were obtained using FEI Tecnai G2 F20 field emission microscopy at an accelerating voltage of 200 kV. X-ray photoelectron spectroscopy (XPS) was tested on Kratos Analytical Ltd—Axis Ultra DLD spectrometer equipped with an Al Kα X-ray source (250 W).And the test was carried out with an analyzer pass energy of 188 eV for survey scans and 30 eV for detailed elemental scans. The Bunauer-Emmet-Teller (BET) surface area and pore volume were obtained by using nitrogen adsorption-desorption isotherms at 77 K with DKSH Belsorp-Max equipment. Prior to nitrogen sorption measurement, all samples were pretreated at 150 °C for 10 h. Acid feature of samples was analyzed by temperature programmed desorption of ammonia (NH_3-TPD) and the reduction capacity of samples were analyzed by temperature programmed reduction of H_2 (H_2-TPR) experiment, which were both performed on Micromeritics Chemisorb 2750 gas-adsorption instrument. The sample (about 200 mg) was placed in quartz reactor and pretreated in N_2 at 200 °C for 2 h, then calmed to room temperature at N_2 atmosphere. Subsequently, for NH_3-TPD test, dose 10% NH_3/He onto sample for 30 min then the sample was purged with pure He at 60 °C for 30 min to remove physical adsorbed NH_3, and then heated to 800 °C with a rate of 3 °C/min. For H_2-TPR test, when the pretreated sample was calmed at room temperature, the N_2 was switched to a 10% H_2/Ar. Then the sample was heated to 800 °C with a rate of 10 °C/min. Thermogravimetric (TG) analysis was carried out with materials heated in nitrogen atmosphere at a ramp rate of 10 °C/min to 900 °C.

2.3. Catalytic performance test

Catalytic reaction was performed on a continuous-flow fixed-bed reactor. The catalysts were all pelleted, crushed, and sieved with 20–40 mesh before using for hydrogenation reaction. The react material for HDA was 5 wt% naphthalene dissolved in cyclohexane, and for HDO

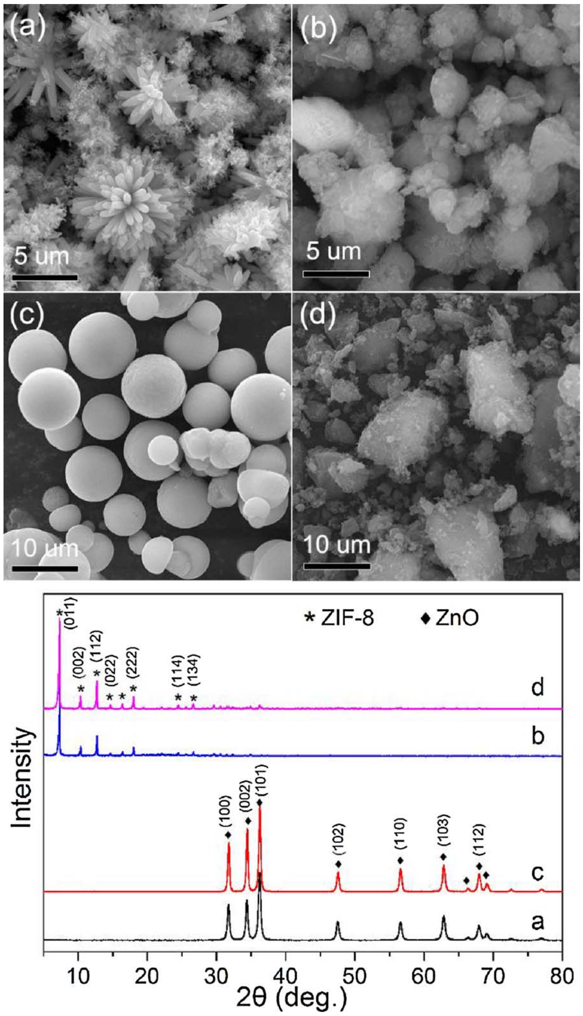

Fig. 2. SEM images and corresponding XRD patterns of (a) flower-shaped ZnO, (b) ZIF-8 synthesized from (a), (c) spherical ZnO, (d) ZIF-8 synthesized from (c).

was 50 wt% methyl palmitate dissolved in decalin. The test conditions were set at 3 MPa, WHSV = 1 h^{-1}, and H_2/oil = 600. Liquid products were collected and analysed with an Agilent 7890A/5975C GC–MS equipped with a HP-5 column.

3. Results and discussion

3.1. Synthesis and structural characterization

In order to express the composition and content of the composites more clearly, the composite was denoted as ZA-n (ZIF-8@Al_2O_3) with n represent different mass percent of Al_2O_3.

In order to observe the changes in the morphology of the reactant and product after the solid state reaction, bulk ZIF-8 samples (Fig. 2b, d) were synthesized from flower-shaped (Fig. 2a), and spherical (Fig. 2c) ZnO, respectively. The ZIF-8 crystals with irregular shape were successfully synthesized, which morphologies are entirely different from those of ZnO precursors. The morphology of ZnO was destroyed totally due to a corrosion of 2-methylimidazole at 180 °C and crystal was reconstructed during reaction. This phenomenon also appeared on ZIF-8@Al_2O_3 composites which will be shown in the later of this paper.

Fig. 3a shows the XRD patterns of ZIF-8, Al_2O_3, and ZIF-8@Al_2O_3 with different percentage of Al_2O_3. The diffraction peaks of ZIF-8 all match well with literature [38]. The two diffraction peaks at 46° and 67° are attributed to γ-Al_2O_3 phase (JCPDF: 1-1308), which were detected on Al_2O_3 and ZA-n (n = 90, 80, 70, 60). Major diffraction peaks

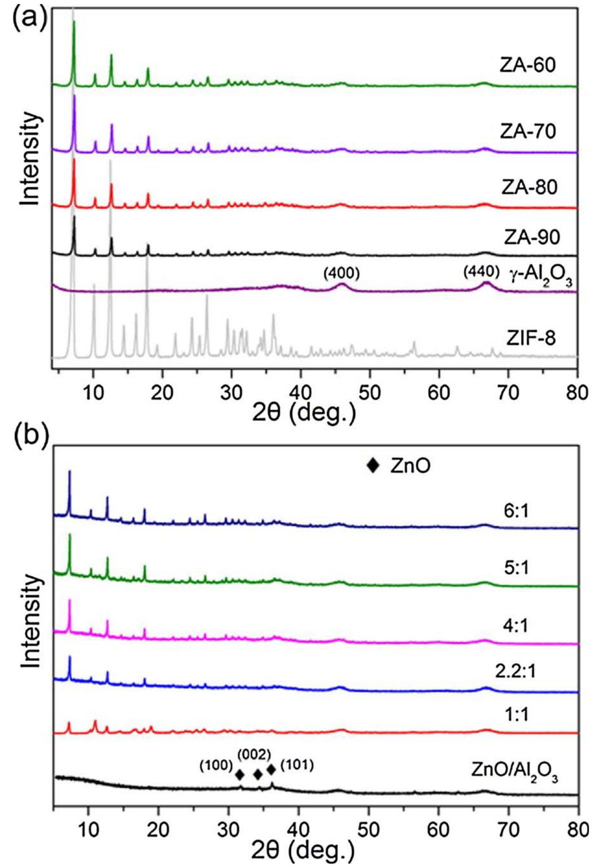

Fig. 3. XRD patterns of (a) ZIF-8@Al_2O_3 with different proportion of Al_2O_3, (b) the synthesized ZA-70 with different molar ratios (2-methylimidazole: ZnO).

of ZA-n are identical with that of ZIF-8 phase, emphasizing successful preparation of ZIF-8 incorporation into matrix Al_2O_3. As we can see, compared with ZIF-8, the intensity of the main diffraction peak in ZA-n is obviously reduced, which is more obvious with the increase of Al_2O_3 content. The intensity decline and shape broadening of diffraction peaks may be due to the reduced size of the ZIF-8 crystal particles in ZA-n composites.

It is well known that the molar ratio of organic ligand and metal salt has a remarkable effect on the synthesis of MOFs. To study the effect of the molar ratio of organic ligand and metal salt on the product, various samples were synthesized at different molar ratios using Al_2O_3 as support (Fig. 3b). The precursor of ZnO/Al_2O_3 (70 wt% Al_2O_3) has only three weak diffraction peaks (at about 2θ = 32°, 34°, and 36°) attributed to hexagonal ZnO structure (JCPDF: 1-1136). The XRD results of composites show that diffraction peaks of ZIF-8 were detected when the molar ratio was 2.2: 1, but weak diffraction peaks of ZnO were also detected. The intensity of diffraction peaks of ZIF-8 reaches its maximum value when the molar ratio was 5: 1, and no obvious peaks of ZnO was detected. The above results indicate that the synthesis of ZA-n composite requires a higher molar ratio than that of pure ZIF-8, which might be explained by that ZnO was in pores of Al_2O_3 support and cannot fully contact and react with 2-methylimidazole when the molar ratio was small.

Fig. 4 shows the SEM images of ZIF-8, Al_2O_3, and ZA-n. Similar to the previously published literature [37], the ZIF-8 synthesized using solid phase method does not have a specific morphology and particle size (Fig. 4a). Only a few particles can be seen as a rhombic dodecahedron structure. For alumina, it has an amorphous structure aggregated with small particles (Fig. 4b). The crystal structure of ZIF-8 could not be observed from SEM images in the ZA-n (Fig. 4c–e), which might be caused by ZIF-8 component was embedded in Al_2O_3 support.

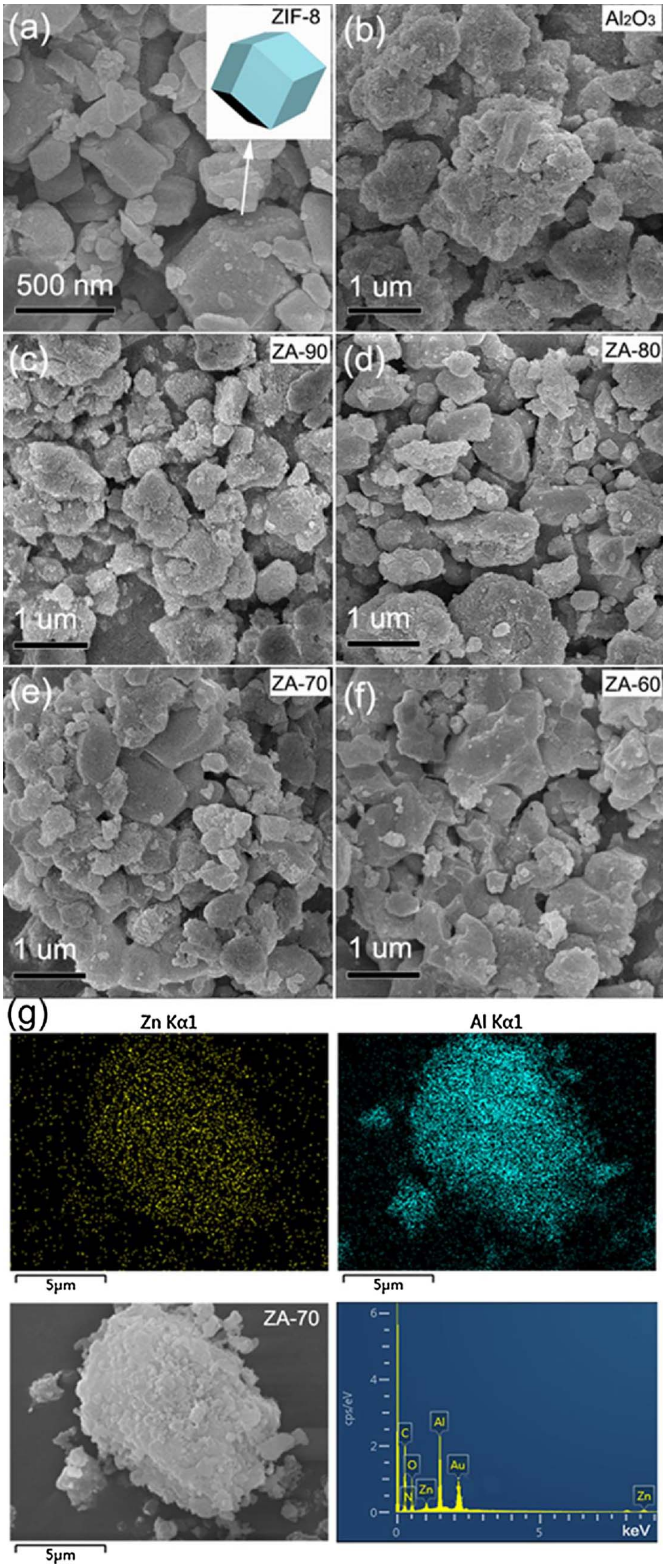

Fig. 4. SEM images of (a) ZIF-8, (b) Al_2O_3, (c) ZA-90, (d) ZA-80, (e) ZA-70, (f) ZA-60 and (g) elemental mapping images of ZA-70.

The elemental mapping results of ZA-70 (Fig. 4g) show that a homogeneous distribution of Al and Zn in ZIF-8@Al_2O_3 composite, which also indicates that the Al_2O_3 support makes the ZIF-8 well dispersed.

As shown in Fig. 5, the morphologies of Al_2O_3, ZIF-8, and ZA-n were also characterized using TEM. ZIF-8 (Fig. 5b) have polygonal crystalline shapes which are consistent with the previous reports [37]. And the pristine Al_2O_3 (Fig. 5a) nanorods were accumulated which lead to a mesoporous structure of particles. The composite components (ZIF-8

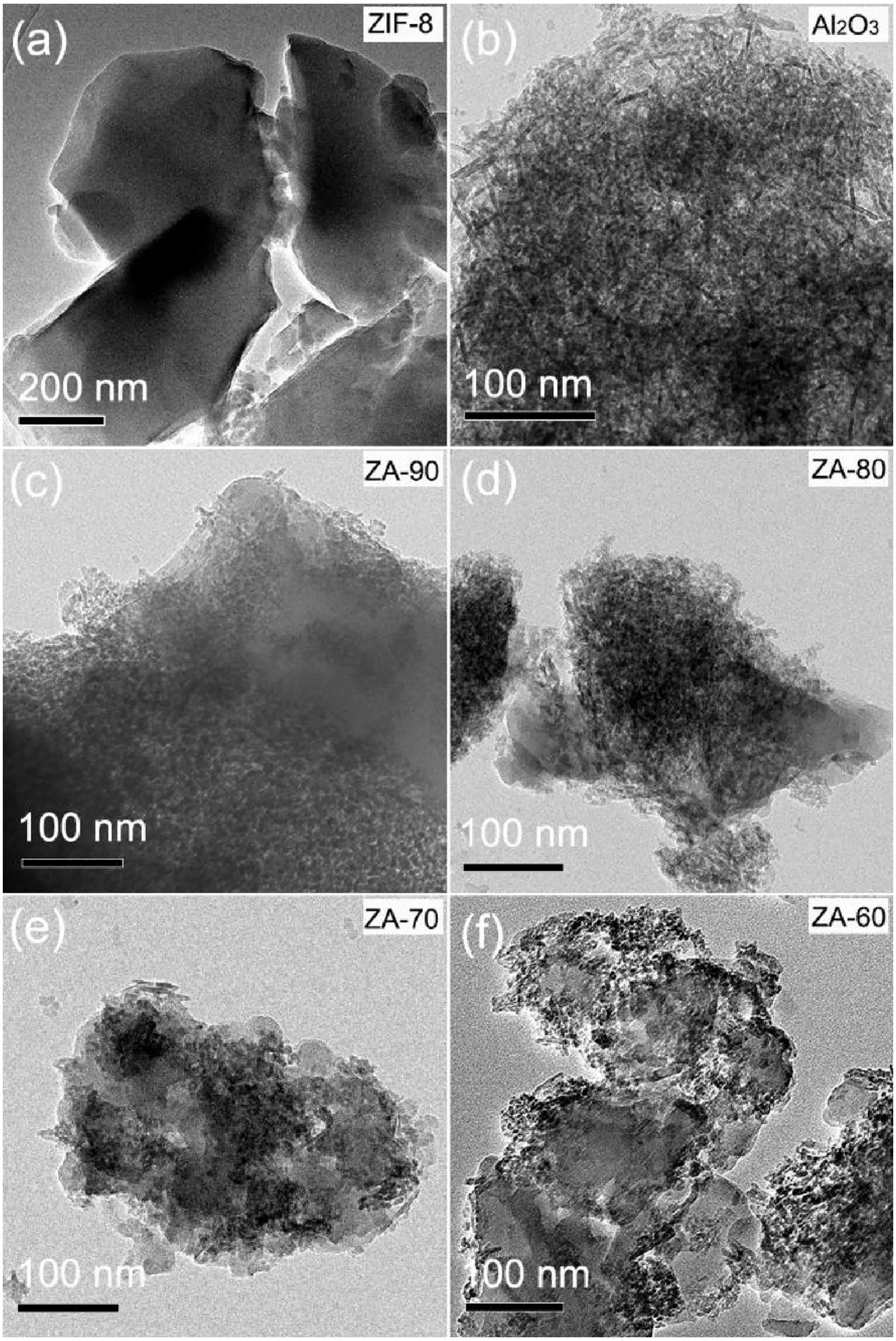

Fig. 5. TEM images of (a) ZIF-8, (b) Al_2O_3, (c) ZA-90, (d) ZA-80, (e) ZA-70 and (f) ZA-60.

with Al_2O_3) are clearly visible in ZA-n (Fig. 5c–f), and almost no large particles of ZIF-8 was observed. Notably, ZIF-8 crystal tended to an inter-connected relationship with Al_2O_3 matrix. That is likely ascribed to the ZIF-8 growth attached to Al_2O_3 support by the abundant hydroxyl groups. As we know, ZnO nanopaticles can be well dispersed on Al_2O_3 support through wetness impregnation method [1,39]. Interestingly, it seems that ZIF-8 linked and connected with each other, which is entirely different from the distribution of ZnO. That is because there was a destruction of ZnO reactant during solid reaction process, as illustrated in Fig. 2.

To analyze porous structure, nitrogen adsorption-desorption of ZA-n composites, Al_2O_3, and pure ZIF-8 were conducted (Fig. 6a). And the porous structure parameters of samples are calculated from N_2 sorption isotherms and listed in Table 1. Isotherm of Al_2O_3 belongs to type IV classification, which shows a hysteresis loop typical of mesoporous materials due to the desorption process. ZIF-8 exhibits a type I isotherm characteristic of microporous. Interestingly, sorption isotherms of ZA-n composites can be viewed as a hybrid of type IV and type I, indicating the coexistence of micropore and mesopore. A sharp increase of nitrogen adsorption at low relative pressure (P/P_0) region indicates the presence of micropore originating from ZIF-8. ZA-n samples show a full evolution of mesoporosity as the Al_2O_3 ratio decreased from 90 to 60. Isotherms of ZA-n all exhibits a narrow hysteresis loop, and the loop becomes slightly narrower with the decrease of Al_2O_3 ratio, which

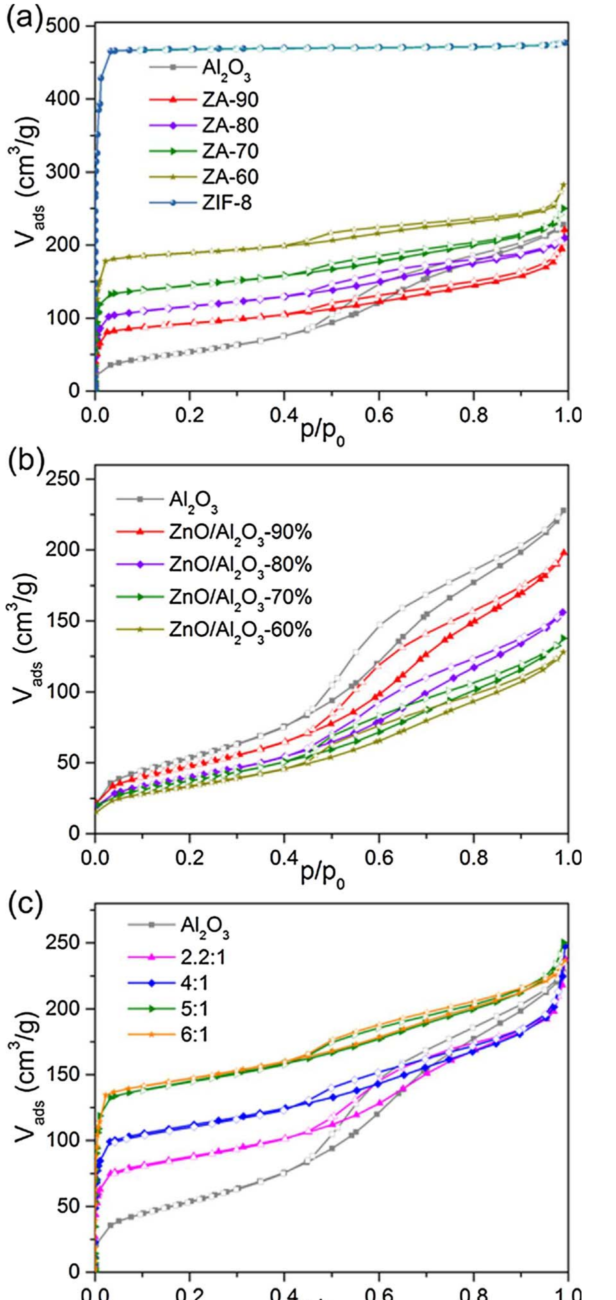

Fig. 6. Nitrogen adsorption-desorption isotherms of (a) ZIF-8@Al_2O_3 with different proportion of Al_2O_3, (b) ZnO/Al_2O_3 with different proportion of Al_2O_3, and (c) ZA-70 with different molar ratios (2-methylimidazole: ZnO).

indicates the decreasing of mesoporosity.

As listed in Table 1, textural parameters of pure ZIF-8 agree well with the published literature [36]. The BET surface area of ZA-n increased with the content of Al_2O_3 decreasing, which was contributed by large microporosity of ZIF-8. For porous volume, microporous volume increased and mesoporous volume decreased with the content of Al_2O_3 decreasing. These results indicate that a meso-microporous composite system has been achieved, which microporosity and/or content of ZIF-8 can easily be tuned by simply adjusting the loading of ZnO in precursor.

To analyze the relationship between ZnO and Al_2O_3 support in ZnO/Al_2O_3-n, nitrogen adsorption-desorption of Al_2O_3 and ZnO/Al_2O_3-n were also compared in Fig. 6b. All the samples show a hysteresis loop only characteristic of mesoporous. And the hysteresis loop becomes slightly narrower with the decrease of Al_2O_3 ratio from 100% to 60%,

Table 1
Textural properties of Al_2O_3, ZA-n, ZnO/Al_2O_3-n, ZIF-8@Al_2O_3-70 prepared by 2-methylimidazole: ZnO feeding molar ratios 2.2: 1, 4: 1, 5: 1, and 6: 1, and ZIF-8.

Sample	S_{BET}[a] (m^2/g)	V_{total}[b] (cm^3/g)	V_{Micr}[c] (cm^3/g)	V_{Mes}[d] (cm^3/g)
Al_2O_3	199	0.35	–	0.35
ZA-90	448	0.35	0.18	0.17
ZA-80	455	0.38	0.21	0.17
ZA-70	588	0.39	0.23	0.14
ZA-60	631	0.36	0.24	0.11
ZnO/A-90[e]	173	0.31	–	0.31
ZnO/A-80	145	0.24	–	0.24
ZnO/A-70	136	0.21	–	0.21
ZnO/A-60	123	0.20	–	0.20
ZA-2.2:1	327	0.35	0.20	0.15
ZA-4:1	436	0.36	0.19	0.15
ZA-6:1	588	0.37	0.24	0.13
ZA-8:1	601	0.36	0.24	0.12
ZIF-8	1660	0.59	0.58	0.01

SBET[a] – BET surface area; Vtotal[b] – total pore volume obtained at $P/P_0 = 0.99$; VMicr[c] – micropore volume calculated by t-plot analysis; VMes[d] – mesopore volume calculated by subtracting the VMicr from Vtotal. ZnO/A-n[e] – ZnO/Al_2O_3-n, and n represent different mass percent of Al_2O_3.

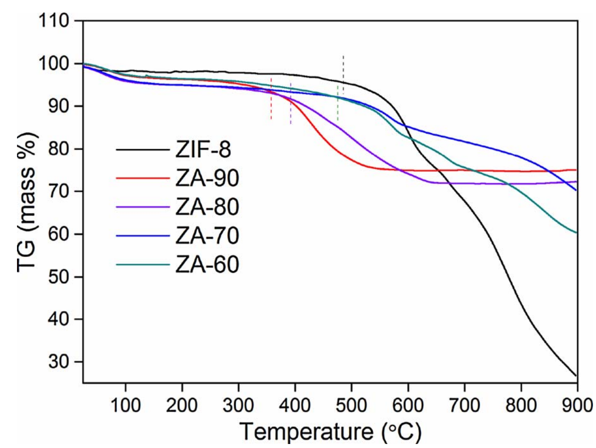

Fig. 7. TG analysis of ZIF-8, ZA-90, ZA-80, ZA-70 and ZA-60.

which indicates the decreasing of mesoporosity. Mesoporous volume of ZnO/Al_2O_3-90% to 60% listed in Table 1 also in agreement with this result. So we can conclude that ZnO was embedded in the pores of Al_2O_3 support through the incipient wetness impregnation method.

The nitrogen sorption (Fig. 6c and Table 1) of products come from different molar ratio of starting materials (2-methylimidazole and ZnO) was also conducted besides XRD analysis (Fig. 3b). And the optimum 2-methylimidazole: ZnO feeding molar ratio is 5:1, which confirmed by a very similar N_2 sorption behaviors of the products prepared by molar ratios of 5: 1 and 6: 1. When the ratio is less than 5: 1, surface area and micropore volume were increased with the molar ratio increasing. That is because ZnO was in the pores of Al_2O_3 support (analysed in Fig. 6b) and cannot fully contact and react with 2-methylimidazole when the molar ratio was less than 5: 1. This result further indicates the textural structure of ZIF-8@Al_2O_3 composite, which is that ZIF-8 crystallites grow within Al_2O_3 matrix.

TG analysis of ZIF-8 and ZA-n was conducted and the results were shown in Fig. 7. As can be seen, the weight loss curves trend of ZA-n with two stages are almost consistent with that of ZIF-8 during heating procedure. Firstly, a little weight loss of 3% for ZIF-8, and 4%–5% for ZA-n composites were detected at first stage, which is attributed to the removal of water and residual molecules (eg. 2-methylimidazoleand) in ZIF-8. Secondly, a sharp decrease in TG weight is caused by the decomposition of organic linker molecules and collapse of ZIF-8 structure. Compared with ZIF-8, the composite curve has a lower weight loss ratio at the content of thermal-stable Al_2O_3. Moreover, the decomposition

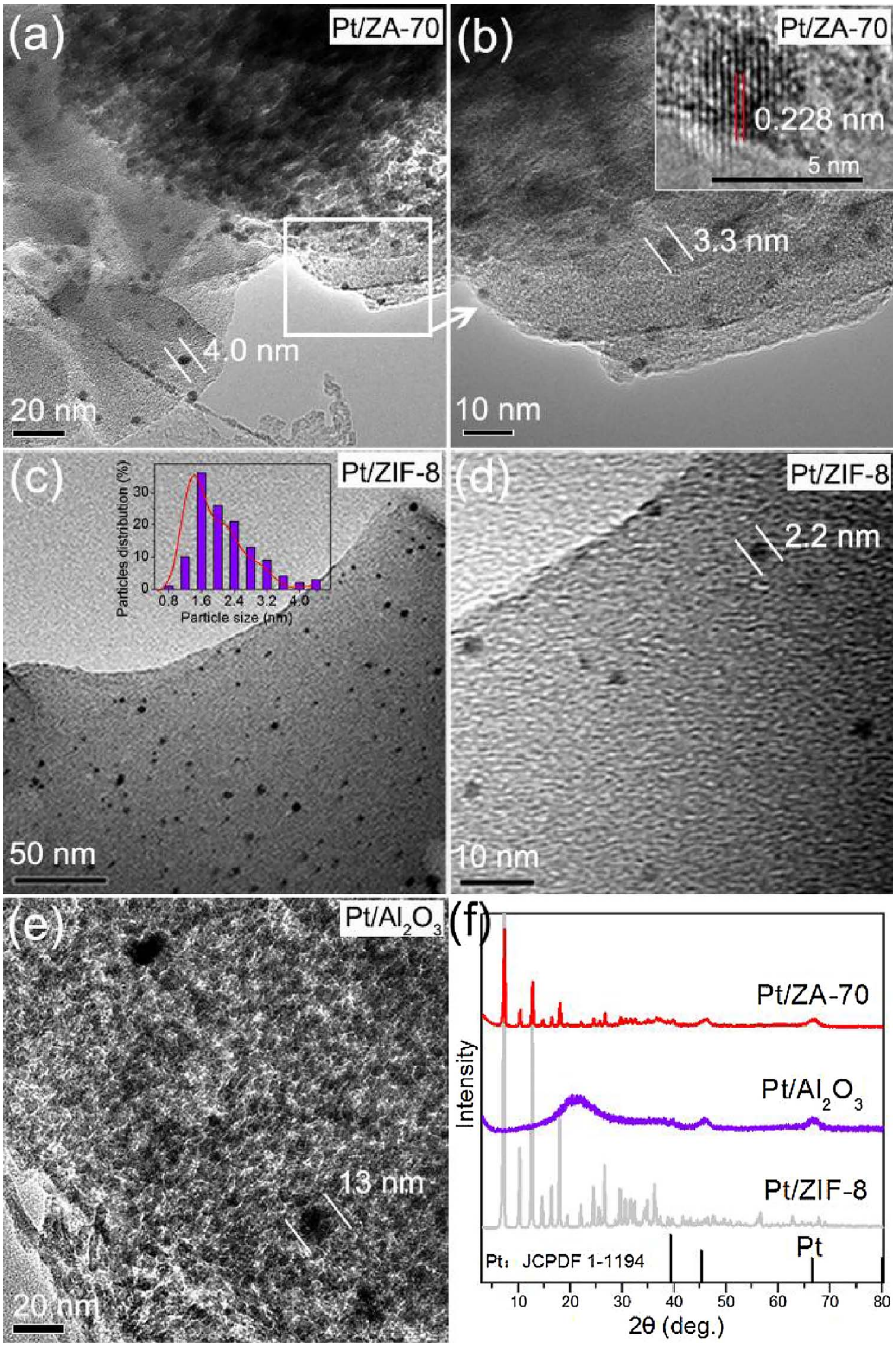

Fig. 8. TEM images of Pt/ZA-70 (a, b), Pt/ZIF-8 (c, d), Pt/Al_2O_3 (e), and XRD (f).

temperature of ZA-70, and ZA-60 are started at around 475 °C which is close to the position of pristine ZIF-8 (485 °C). While composites ZA-90 and ZA-80 exhibit a lower decomposition temperature. That because an apparent activation energy for pure ZIF-8 is higher than that of composite materials, so a faster degradation reaction of ZIF-8 when forming a composite [40]. Especially, decomposition temperature of the composite is decreased with ZIF-8 content decreasing. The final residue, weighing 75.0%, 73.5%, 70.3%, 60.3% and 26.7% for ZA-90, ZA-80, ZA-70, ZA-60, and ZIF-8 respectively. The residue is ZnO, Al_2O_3, and also a little of carbon resulting from carbonization of organic ligand at second stage in the nitrogen atmosphere. It should be noted that because of an incomplete carbonization before 900 °C, so ZA-70, ZA-60, and ZIF-8 have a relative higher weight loss than ZA-90, ZA-80. The above results show that ZIF-8 and ZA-70 can be used at lower than 475 °C, which will not damage its structure.

Porous γ-Al_2O_3 is a frequently used support for hydrogenation catalysts. Hence, the ZA-n composite was used as support to prepare the catalyst and used for hydrogenation reaction. Pt/ZA-70 was synthesized using the incipient wetness impregnation method. Because ZIF-8 is a hydrophobic and not acid resistant MOFs, thus we chose an acetone solution of acetylacetone platinum as an immersion solution, which as much as possible to make Pt enter into the pores of ZIF-8.

The particles size distribution of platinum nanoparticles of Pt/ZA-70 and Pt/ZIF-8 was examined by TEM (Fig. 8). Fig. 8a and b shows the

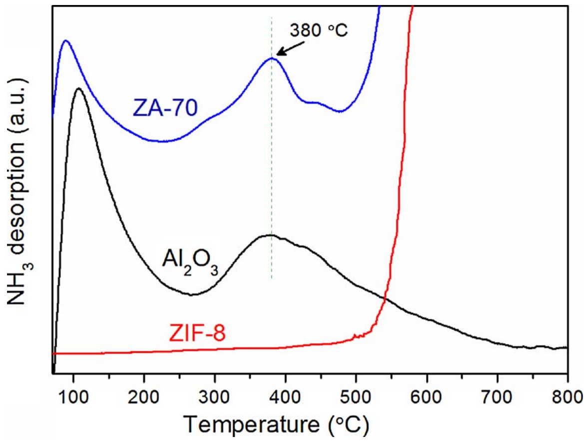

Fig. 9. NH_3-TPD of ZA-70, ZIF-8 and Al_2O_3.

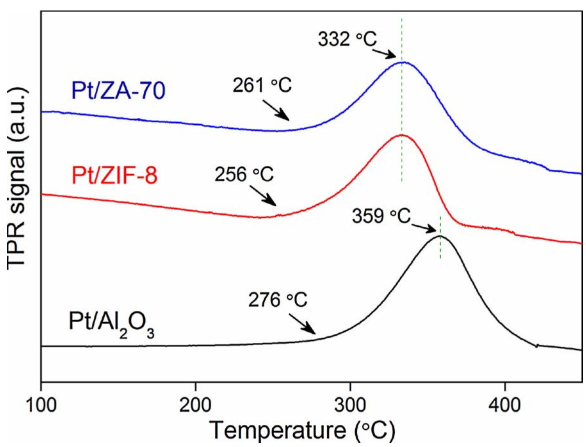

Fig. 10. H_2-TPR of Pt/ZA-70, Pt/ZIF-8 and Pt/Al_2O_3.

TEM images of Pt/ZA-70 catalysts, which indicates Pt nanoparticles in mean size of about 2–4 nm highly dispersed on ZIF-8 component of the composite. The HRTEM image inserted in Fig. 8b indicates that the interplanar spacing for the lattice fringe of is 0.227 nm, which correspond to the (111) lattice plane of the face-centered cubic (fcc) Pt structure [41]. The TEM images of Pt/ZIF-8 (Fig. 8c, d) indicate that highly dispersed Pt nanoparticles can be easily obtained by encapsulation of ZIF-8 using incipient wetness impregnation method. It also shows that acetone solution of acetylacetone platinum is suitable for hydrophobic ZIF-8. However, a lot of large particles with size of about 13 nm appeared in Pt/Al_2O_3 (Fig. 8e). Hence, ZIF-8 component can control a smaller size dispersed metal particles than Al_2O_3.

There is no observation of Pt characteristic peaks on Pt/ZA-70, Pt/Al_2O_3, and Pt/ZIF-8 (Fig. 8f), which should be due to a lower Pt loading (0.7 wt%) and small size of Pt nanoparticles. And the major peaks of Pt/ZA-70 and Pt/ZIF-8 are identical with that of ZIF-8, indicating that introduction of Pt can't destroy structure of ZIF-8.

In addition, X-ray photoelectron energy (XPS) was employed to investigate the catalytic architecture of Pt/ZA. The wide scanning spectra (Fig. S2a) indicates that Pt/ZA is mainly composed of C, N, O, Zn, Al and Pt elements. The spectrum of Pt 4f (Fig. S2b) displays one peak at 70.8 eV, corresponding to the Pt^0 $4f_{5/2}$, further demonstrating the successful encapsulation of Pt nanoparticles in support.

The acid properties of ZIF-8, Al_2O_3 and ZA-70 were determined by NH_3-TPD (Fig. 9). Taking into account the thermal stability of ZIF-8, the temperature of NH_3-TPD for ZIF-8 and ZA-70 is up to 580 °C. Note that a sharp increase in NH_3-TPD curve start at about 480 °C due to collapse of ZIF-8 structure and decomposition of organic linker molecules, which is in accordance with the result of TG result (Fig. 7). The ZA-70

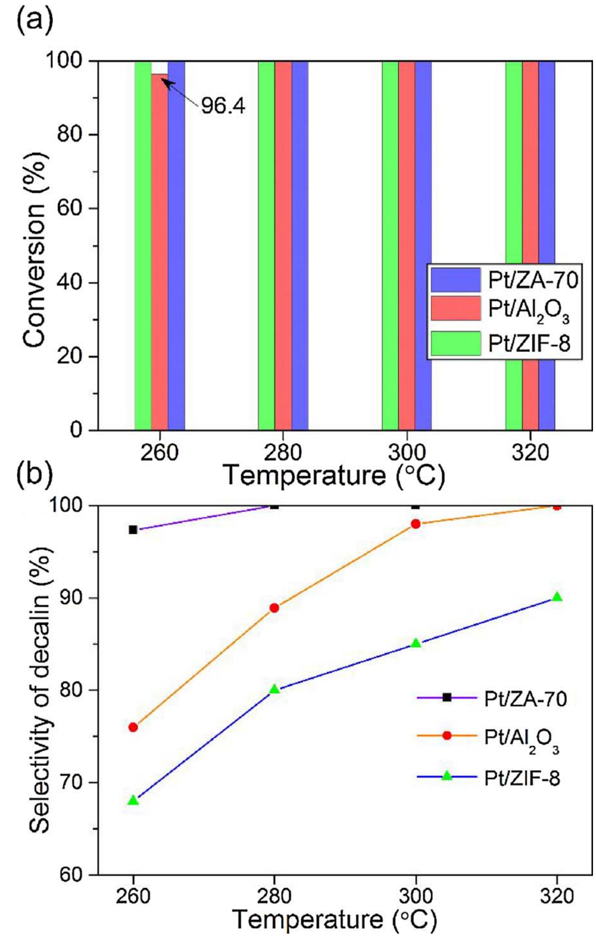

Fig. 11. Conversion and decalin selectivity over Pt/ZA-70, Pt/Al_2O_3, and Pt/ZIF-8 catalysts at different temperature.

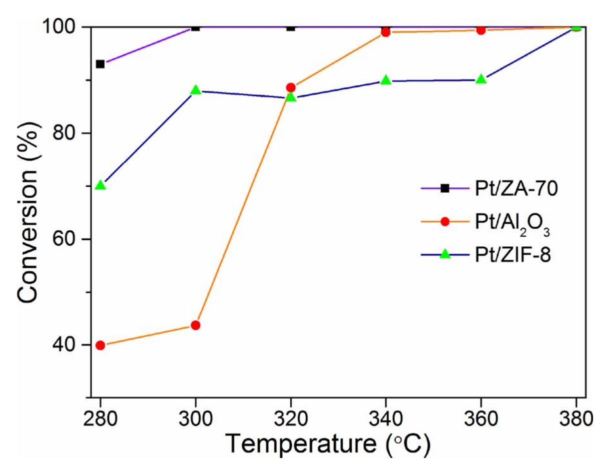

Fig. 12. Conversion of Pt/ZA-70, Pt/Al_2O_3, and Pt/ZIF-8 catalysts at different temperature in HDO reaction.

composite and ZIF-8 exhibited an identical desorption peak at 380 °C, which corresponding to intermediate acidic sites. While ZIF-8 sample has no peak in this range. Thus, there are a lot of medium acid sites on ZA-70, which comes from the contribution of Al_2O_3 component and may play a critical role in activity and product selectivity during hydrogenation reaction [42].

The H_2-TPR results show that acetylacetone platinum can be reduced by H_2 at no more than 400 °C (Fig. 10). It is interesting to note that comparing with the Pt/Al_2O_3, the reduction peak of Pt/ZIF-8 and

Table 2
Product selectivity of Pt/ZA-70, Pt/Al_2O_3, and Pt/ZIF-8 catalyst at different temperature in HDO reaction.

Products (%)	Catalysts	380 °C	360 °C	340 °C	320 °C	300 °C	280 °C
Hexadecane	Pt/ZA	91.2	15.5	8.4	1.4	0	0
	Pt/A	24.4	27.2	34.2	32.4	16.3	2.0
	Pt/Z	12.2	8.3	4.1	2.1	0	0
Hexadecene	Pt/ZA	0	70.1	65.2	60.3	42.0	36.4
	Pt/A	0	0	0	0	0	0
	Pt/Z	0	0	0	0	0	0
Pentadecane	Pt/ZA	3.6	2.5	1.8	1.3	0	0
	Pt/A	73.9	70.3	63.2	49.1	36.3	8.1
	Pt/Z	0	0	0	0	0	0
Hexadecanol	Pt/ZA	0	8.7	20.0	28.1	55.2	61.4
	Pt/A	0	0	0	0	0	0
	Pt/Z	73.2	70.3	67.1	66.3	30.9	15.2
Hexadecanal	Pt/ZA	0	0	0	0	0	0
	Pt/A	0	0	0	1.2	14.4	18.3
	Pt/Z	10.1	8.0	2.2	0	0	0
Palmitic acid	Pt/ZA	0	0	0	0	0	0
	Pt/A	0	0	0	11.4	29	66.3
	Pt/Z	0	7.8	19	18.6	57.8	65.1
Others	Pt/ZA	5.2	3.2	4.6	8.9	2.8	2.2
	Pt/A	1.7	2.5	2.6	5.9	4.0	5.3
	Pt/Z	4.5	5.6	7.6	13	11.3	19.7

Pt/ZA: Pt/ZA-70; Pt/A: Pt/Al_2O_3; Pt/Z: Pt/ZIF-8.

Pt/ZA-70 samples is apparently shifted to a lower temperature. The reduction peaks of Pt/ZA-70 and Pt/ZIF-8 are the same and 27 °C lower than that of Pt/Al_2O_3, implying that a smaller size and higher dispersion of Pt particles on ZIF-8 support. This result agrees well with TEM images in Fig. 8. In this paper, all the catalysts were reduced by H_2 at 350 °C for 1 h to insure the reduction of Pt^{2+} before hydrogenation reaction.

Finally, it is noted that our approach doesn't involve any solvent and pretreatment. ZnO can achieve by wetness impregnation of zinc nitrate. So this approach may not be limited to ZIF-8@Al_2O_3 materials, which holds promising to synthesize other porous support with ZIF-8.

3.2. Hydrogenation over Pt/ZA catalysts

Considering the properties of ZIF-8@Al_2O_3, 0.7 wt% Pt/ZA-70 catalyst was synthesized and its catalysis behavior was tested using hydrogenation reaction. In this work, Pt/ZA-70 was used as catalyst in HDA of naphthalene and HDO of methyl palmitate, respectively. For comparison, 0.7 wt% Pt/ZIF-8 and 0.7 wt% Pt/Al_2O_3 were also tested under identical conditions.

Catalytic activity of Pt/ZA-n was firstly studied in HDA of naphthalene, in which decalin (including *trans*-decalin and *cis*-decalin) was the main product and tetralin was the by-product. As illustrated in Fig. 11a, all catalysts exhibit high conversion of naphthalene from 260 to 320 °C. Pt/Al_2O_3 showed the lowest activity, which conversion of naphthalene was 96.4% at 260 °C. However, the conversion of naphthalene does not accurately reflect the activity of different catalysts. For HDA of naphthalene, the selectivity of decalin is most likely to accurately reflect the activity of the catalyst. Clearly, with ZIF-8 being incorporated in Al_2O_3, the decalin selectivity have been enhanced compared with its pristine components (ZIF-8 and Al_2O_3). Pt/ZA-70 showed the highest selectivity of decalin, which was 97.3% even at 260 °C. However, the selectivities of decalin for Pt/Al_2O_3 and Pt/ZIF-8 at 260 °C were only 76% and 68%, respectively (Fig. 11b).

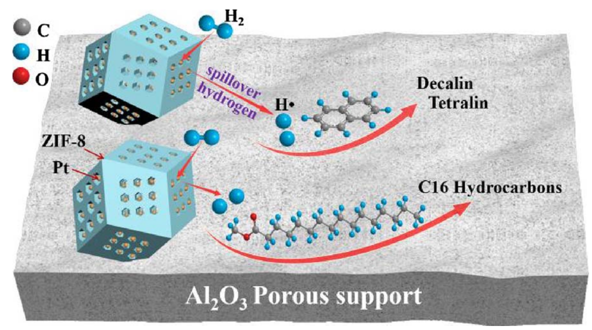

Fig. 14. Reaction pathway for the hydrodeoxygenation of Pt/ZA-70.

As previously published reports, the HDA of naphthalene relied on amounts of active sites as well as surface acid properties [43–45]. Tetralin is just an incompletely hydrogenated intermediate in HDA reaction. As analyzed by TEM (Fig. 8), Pt nanoparticles are dispersed uniformly in ZIF-8 component due to the "confinement effect" of MOFs, but its selectivity of decalin is the lowest. So the high decalin selectivity for Pt/ZA-70 catalyst generated not only from highly dispersed Pt nanoparticles, but also from acid property of Al_2O_3 component.

For another type of hydrogenation reaction, HDO of methyl palmitate was also investigated for Pt/ZA-70, Pt/Al_2O_3, and Pt/ZIF-8, respectively. As shown in Fig. 12, Pt/ZA-70 shows the highest conversion of methyl palmitate, which conversion was 93% even at 280 °C. However, the conversion of methyl palmitate for Pt/Al_2O_3 and Pt/ZIF-8 at 280 °C were only 39.9% and 70%, respectively. Product selectivities of various catalysts at different temperature in HDO reaction were listed in Table 2. Although Pt/ZIF-8 have a high conversion, but hydrocarbon selectivity was lower than 12.2% in measured temperature range. The major product of Pt/ZIF-8 is hexadecanol, which is an intermediate in HDO reaction.

According to our previous studies, there are two distinct pathways for deoxygenation for methyl palmitate. One is the cleavage of C—O bond and hydrogenation to produce hexadecane (HDO), and the other is the cleavage of C—C bond and decarbonylation to produce pentadecane (DCO) [46,47]. Acid properties of catalyst play a crucial role in hydrogenation activity and cracking activity for supported metal

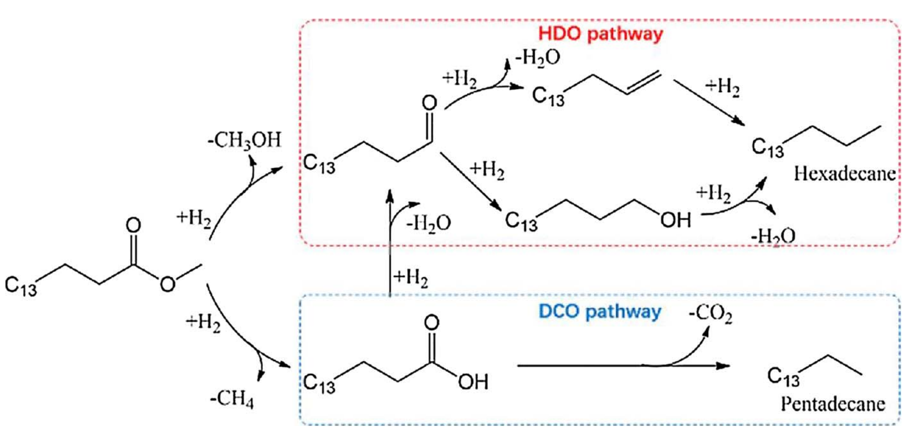

Fig. 13. Reaction pathway for the HDO of methyl palmitate.

catalysts. High acidity of support can make the catalyst more selective towards C—C bond cleavage, and acidity also is important for the transformation of hexadecanol to hexadecane [48]. Detailed process of the two reaction pathways were concluded in Fig. 13.

It is noteworthy to mention that a significant change in product selectivity can be observed for Pt/ZA-70, Pt/Al_2O_3, and Pt/ZIF-8 (Table 2). As we can see, very few of hydrocarbon product was obtained on Pt/ZIF-8 in the whole temperature range. The dominate product is an intermediate hexadecanol, which might attribute to no acidity of ZIF-8. The catalyst cannot effectively adsorb the reactant molecules due to the absence of acidity, which will greatly reduce the catalytic activity. Conversely, major products obtained by catalyst Pt/ZA-70 above 320 °C were hexadecene and hexadecane. When reaction temperature reached 380 °C, hexadecane (up to 91.2%) becomes the main product, because higher temperature leads to the further hydrogenation of hexadecene to hexadecane. The excellent selectivity of hexadecane indicates that HDO almost was the only reaction pathway for Pt/ZA-70 catalyst. Whereas Pt/Al_2O_3 yield dominant products were pentadecane and hexadecane, implying that DCO was the dominant reaction pathway, and also exists part of the HDO reaction pathway (Fig. 13).

The above results indicate that Pt/ZA-70 catalyst is more favorable for HDO pathway than DCO pathway, which might because most of the Pt nanoparticles were encapsulated in the pores of ZIF-8 and the acidic sites on the ZA-70 surface might play the role of adsorption reactant molecules. A possible bi-functional mechanism scheme was proposed to explain the effect of Pt/ZA-70 in hydrogenation, in which the ZA composite can simultaneously exert the advantages of ZIF-8 and Al2O3 support. The micropores of ZIF-8 can increase the dispersion of Pt nanoparticles with smaller size. At the same time, the functional groups on the surface of $Al2O_3$ accompany with its mesoporous structure can improve the selectivity of the product. In this way, ZIF-8@Al_2O_3 composite have significantly improved utilization efficiency of both ZIF-8 and Al_2O_3 components. The detailed process of catalysis mechanism was illustrated in Fig. 14. H_2 molecules were adsorbed by ZIF-8 component with high surface area, and then were activated and dissociated to active H atoms by Pt nanoparticles. Subsequently, these activated H atoms were transferred to adjacent Al_2O_3 component to react with reactant molecules due to the "spillover hydrogen effect"[49,50]. Simultaneously, reactant molecules can be adsorbed by acidic sites of Al_2O_3, which are free access to mesoporous of Al_2O_3 and cannot enter into the pores of ZIF-8 limited by its microporous structure. Consequently, the composite system results in an increase of catalytic efficiency, and consequently improves catalytic activity and selectivity.

Notably, the confinement function of ZIF-8 component not only result in high dispersion of Pt nanoparticles, but also limit the growth of Pt nanoparticles under high reaction temperature. Additionally, the microporous structure and the non-acid sites of ZIF-8 can reduce the adsorption of reactant molecules in the pores, which might prevent the poisoning of Pt nanoparticles and coke formation. Hence, this kind of composite material might show completely different properties in various catalytic reaction.

4. Conclusions

In conclusion, a new strategy was proposed to synthesize a novel composite of ZIF-8 embedded in porous Al_2O_3 by a solvent-free solid-state method. In this method, supported zinc oxide was used as a precursor, and dimethyl imidazole was used as an organic ligand. Series of ZIF-8@Al_2O_3 were synthesized arising from the crystal growth of ZIF-8 on Al_2O_3 supports. BET results reveal that the distribution of micropores and mesopores can be controlled easily by simply adjusting the amount of zinc salt impregnated into porous Al_2O_3 support. Additionally, the particle size of ZIF-8 crystal was significantly reduced due to its being embedded in porous support. It is also important to note that this approach doesn't involve any surfactants, solvent and pretreatment process, which holds promising to synthesize other porous support with ZIF-8. Pt/ZA-70 catalyst exhibits high activity and selectivity compared to Pt/Al_2O_3 and Pt/ZIF-8 in HDA and HDO reactions. For HDA of naphthalene, the high decalin selectivity for Pt/ZA-70 composite generated not only from highly dispersed Pt nanoparticles, but also from acid property of Al_2O_3 component. For HDO of methyl palmitate, the GC–MS results indicate that HDO almost the only reaction pathway for Pt/ZA-70 catalyst. Conversely, DCO was the dominant reaction pathway for Pt/Al_2O_3 catalyst, which also exists part of the HDO reaction pathway. Finally, the experimental results show that there is a significant spillover hydrogen effect in the hydrogenation reaction for Pt/ZA-n catalyst. The special structure of the composite material might show completely different properties in various catalytic reaction.

Acknowledgements

This work was financially supported by the NSFC (21603107, 21376123, U1403293), NSFT (15JCQNJC05500, 16YFZCGX00020), MOE (IRT-13R30 and 113016A), and the Research Fund for 111 Project (B12015).

Appendix A. Supplementary data

Supplementary data associated with this article can be found, in the online version, at https://doi.org/10.1016/j.apcatb.2018.01.022.

References

[1] A. López-Benítez, G. Berhault, A. Guevara-Lara, NiMo catalysts supported on Mn-Al_2O_3 for dibenzothiophene hydrodesulfurization application, Appl. Catal. B: Environ. 213 (2017) 28–41.
[2] T. Araya, M. Jia, J. Yang, P. Zhao, K. Cai, W. Ma, Y. Huang, Resin modified MIL-53 (Fe) MOF for improvement of photocatalytic performance, Appl. Catal. B: Environ. 203 (2017) 768–777.
[3] M. Yurderi, A. Bulut, M. Zahmakiran, M. Gülcan, S. Özkar, Ruthenium(0) nanoparticles stabilized by metal-organic framework (ZIF-8): highly efficient catalyst for the dehydrogenation of dimethylamine-borane and transfer hydrogenation of unsaturated hydrocarbons using dimethylamine-borane as hydrogen source, Appl. Catal. B: Environ. 160–161 (2014) 534–541.
[4] I.E. Ertas, M. Gulcan, A. Bulut, M. Yurderi, M. Zahmakiran, Metal-organic framework (MIL-101) stabilized ruthenium nanoparticles: highly efficient catalytic material in the phenol hydrogenation, Microporous Mesoporous Mater. 226 (2016) 94–103.
[5] M. Gulcan, M. Zahmakiran, S. Özkar, Palladium(0) nanoparticles supported on metal organic framework as highly active and reusable nanocatalyst in dehydrogenation of dimethylamine-borane, Appl. Catal. B: Environ. 147 (2014) 394–401.
[6] D. Ji, H. Zhou, Y. Tong, J. Wang, M. Zhu, T. Chen, A. Yuan, Facile fabrication of MOF-derived octahedral CuO wrapped 3D graphene network as binder-free anode for high performance lithium-ion batteries, Chem. Eng. J. 313 (2017) 1623–1632.
[7] G. Zhou, M.F. Wu, Q.J. Xing, F. Li, H. Liu, X.B. Luo, J.P. Zou, J.M. Luo, A.Q. Zhang, Synthesis and characterizations of metal-free semiconductor/MOFs with good stability and high photocatalytic activity for H_2 evolution: a novel Z-scheme heterostructured photocatalyst formed by covalent bonds, Appl. Catal. B: Environ. 220 (2018) 607–614.
[8] H. Liu, J. Zhang, D. Ao, Construction of heterostructured $ZnIn_2S$@NH_2-MIL-125(Ti) nanocomposites for visible-light-driven H_2 production, Appl. Catal. B: Environ. 221 (2018) 433–442.
[9] L. Dong, M. Chen, J. Li, D. Shi, W. Dong, X. Li, Y. Bai, Metal-organic framework-graphene oxide composites: a facile method to highly improve the CO_2 separation performance of mixed matrix membranes, J. Membr. Sci. 520 (2016) 801–811.
[10] G. Zhou, M.F. Wu, Q.J. Xing, F. Li, H. Liu, X.B. Luo, J.P. Zou, J.M. Luo, A.Q. Zhang, Synthesis and characterizations of metal-free semiconductor/MOFs with good stability and high photocatalytic activity for H_2 evolution: a novel Z-scheme heterostructured photocatalyst formed by covalent bonds, Appl. Catal. B: Environ. 220 (2018) 607–614.
[11] J. Liu, R. Li, Y. Hu, T. Li, Z. Jia, Y. Wang, Y. Wang, X. Zhang, C. Fan, Harnessing Ag nanofilm as an electrons transfer mediator for enhanced visible light photocatalytic performance of Ag@AgCl/Ag nanofilm/ZIF-8 photocatalyst, Appl. Catal. B: Environ. 202 (2017) 64–71.
[12] S. Liu, F. Chen, S. Li, X. Peng, Y. Xiong, Enhanced photocatalytic conversion of greenhouse gas CO_2 into solar fuels over g-C_3N_4 nanotubes with decorated transparent ZIF-8 nanoclusters, Appl. Catal. B: Environ. 211 (2017) 1–10.
[13] L. Pan, T. Muhammad, L. Ma, Z.F. Huang, S. Wang, L. Wang, J.J. Zou, X. Zhang, MOF-derived C-doped ZnO prepared via a two-step calcination for efficient photocatalysis, Appl. Catal. B: Environ. 189 (2016) 181–191.
[14] Y. Zhang, X. Bo, C. Luhana, H. Wang, M. Li, L. Guo, Facile synthesis of a Cu-based

MOF confined in macroporous carbon hybrid material with enhanced electrocatalytic ability, Chem. Commun. (Camb) 49 (2013) 6885–6887.
[15] S. Pourebrahimi, M. Kazemeini, L. Vafajoo, Embedding graphene nanoplates into MIL-101(Cr) pores: synthesis, characterization, and CO_2 adsorption studies, Ind. Eng. Chem. Res. 56 (2017) 3895–3904.
[16] A. Dhakshinamoorthy, A.M. Asiri, H. Garcia, Metal organic frameworks as versatile hosts of Au nanoparticles in heterogeneous catalysis, ACS Catal. 7 (2017) 2896–2919.
[17] P. Tan, G. Li, R. Fang, L. Chen, R. Luque, Y. Li, Controlled growth of monodisperse ferrite octahedral nanocrystals for biomass-derived catalytic applications, ACS Catal. 7 (2017) 2948–2955.
[18] L. Zeng, X. Guo, C. He, C. Duan, Metal-organic frameworks versatile materials for heterogeneous photocatalysis, ACS Catal. 6 (2016) 7935–7947.
[19] N. Wei, Y. Zhang, L. Liu, Z.B. Han, D.Q. Yuan, Pentanuclear Yb(III) cluster-based metal-organic frameworks as heterogeneous catalysts for CO_2 conversion, Appl. Catal. B: Environ. 219 (2017) 603–610.
[20] L. Ai, C. Zhang, L. Li, J. Jiang, Iron terephthalate metal-organic framework: revealing the effective activation of hydrogen peroxide for the degradation of organic dye under visible light irradiation, Appl. Catal. B: Environ. 148–149 (2014) 191–200.
[21] N. Wei, Y. Zhang, L. Liu, Z.B. Han, D.Q. Yuan, Pentanuclear Yb(III) cluster-based metal-organic frameworks as heterogeneous catalysts for CO_2 conversion, Appl. Catal. B: Environ. 219 (2017) 603–610.
[22] I.E. Ertas, M. Gulcan, A. Bulut, M. Yurderi, M. Zahmakiran, Rhodium nanoparticles stabilized by sulfonic acid functionalized metal-organic framework for the selective hydrogenation of phenol to cyclohexanone, J. Mol. Catal. A: Chem. 410 (2015) 209–220.
[23] M. Faustini, J. Kim, G.Y. Jeong, J.Y. Kim, H.R. Moon, W.S. Ahn, D.P. Kim, Microfluidic approach toward continuous and ultrafast synthesis of metal-organic framework crystals and hetero structures in confined microdroplets, J. Am. Chem. Soc. 135 (2013) 14619–14626.
[24] Z. Li, H.C. Zeng, Armored MOFs enforcing soft microporous MOF nanocrystals with hard mesoporous silica, J. Am. Chem. Soc. 136 (2014) 5631–5639.
[25] J. Gorka, P.F. Fulvio, S. Pikus, M. Jaroniec, Mesoporous metal organic framework-boehmite and silica composites, Chem. Commun. (Camb) 46 (2010) 6798–6800.
[26] A.M.B. Furtado, J. Liu, Y. Wang, M.D. LeVan, Mesoporous silica–metal organic composite: synthesis, characterization, and ammonia adsorption, J. Mater. Chem. 21 (2011) 6698.
[27] Z. Karimi, A. Morsali, Modulated formation of metal-organic frameworks by oriented growth over mesoporous silica, J. Mater. Chem. A 1 (2013) 3047.
[28] C. Li, M. Zhang, X. Di, D. Yin, W. Li, C. Liang, One-step synthesis of Pt@ZIF-8 catalyst for the selective hydrogenation of 1,4-butynediol to 1,4-butenediol, Chin. J. Catal. 37 (2016) 1555–1561.
[29] S.N. Zhao, X.Z. Song, S.Y. Song, H.J. Zhang, Highly efficient heterogeneous catalytic materials derived from metal-organic framework supports/precursors, Coord. Chem. Rev. 337 (2017) 80–96.
[30] H. Dai, B. Xia, L. Wen, C. Du, J. Su, W. Luo, G. Cheng, Synergistic catalysis of AgPd@ZIF-8 on dehydrogenation of formic acid, Appl. Catal. B: Environ. 165 (2015) 57–62.
[31] M. Zahmakiran, Iridium nanoparticles stabilized by metal organic frameworks (IrNPs@ZIF-8): synthesis, structural properties and catalytic performance, Dalton Trans. 41 (2012) 12690–12696.
[32] X. Song, Z. Qiu, X. Yang, H. Gong, S. Zheng, B. Cao, H. Wang, H. Möhwald, D. Shchukin, Submicron-lubricant based on crystallized Fe_3O_4 spheres for enhanced tribology performance, Chem. Mater. 26 (2014) 5113–5119.
[33] V.O.O. Gonçalves, P.M. de Souza, V.T. da Silva, F.B. Noronha, F. Richard, Kinetics of the hydrodeoxygenation of cresol isomers over Ni_2P/SiO_2: proposals of nature of deoxygenation active sites based on an experimental study, Appl. Catal. B: Environ. 205 (2017) 357–367.
[34] M. Oregui-Bengoechea, I. Gandarias, N. Miletić, S.F. Simonsen, A. Kronstad, P.L. Arias, T. Barth, Thermocatalytic conversion of lignin in an ethanol/formic acid medium with NiMo catalysts: role of the metal and acid sites, Appl. Catal. B: Environ. 217 (2017) 353–364.
[35] O. Poole, K. Alharbi, D. Belic, E.F. Kozhevnikova, I.V. Kozhevnikov, Hydrodeoxygenation of 3-pentanone over bifunctional Pt-heteropoly acid catalyst in the gas phase: enhancing effect of gold, Appl. Catal. B: Environ. 202 (2017) 446–453.
[36] J.B. Lin, R.B. Lin, X.N. Cheng, J.P. Zhang, X.M. Chen, Solvent/additive-free synthesis of porous/zeolitic metal azolate frameworks from metal oxide/hydroxide, Chem. Commun. (Camb) 47 (2011) 9185–9187.
[37] M. Lanchas, D. Vallejo-Sanchez, G. Beobide, O. Castillo, A.T. Aguayo, A. Luque, P. Roman, A direct reaction approach for the synthesis of zeolitic imidazolate frameworks: template and temperature mediated control on network topology and crystal size, Chem. Commun. (Camb) 48 (2012) 9930–9932.
[38] K.S. Park, Z. Ni, A.P. Côté, J.Y. Choi, R. Huang, F.J. Uribe-Romo, H.K. Chae, M. O'Keeffe, O.M. Yaghi, Exceptional chemical and thermal stability of zeolitic imidazolate frameworks, Proc. Natl. Acad. Sci. U. S. A. 103 (2006) 10186–10191.
[39] J.A. Botas, D.P. Serrano, A. García, J. de Vicente, R. Ramos, Catalytic conversion of rapeseed oil into raw chemicals and fuels over Ni- and Mo-modified nanocrystalline ZSM-5 zeolite, Catal. Today 195 (2012) 59–70.
[40] F. Cacho-Bailo, C. Tellez, J. Coronas, Interactive thermal effects on metal-organic framework polymer composite membranes, Chemistry 22 (2016) 9533–9536.
[41] Y. Hu, Y. Liu, Y. Sun, Mesoporous colloidal superparticles of platinum-group nanocrystals with surfactant-free surfaces and enhanced heterogeneous catalysis, Adv. Funct. Mater. 25 (2015) 1638–1647.
[42] L. Zhang, W. Fu, Q. Yu, T. Tang, Y. Zhao, Y. Li, Effect of citric acid addition on the morphology and activity of Ni_2P supported on mesoporous zeolite ZSM-5 for the hydrogenation of 4,6-DMDBT and phenanthrene, J. Catal. 345 (2017) 295–307.
[43] G. Yun, Q. Guan, W. Li, The synthesis and mechanistic studies of a highly active nickel phosphide catalyst for naphthalene hydrodearomatization, RSC Adv. 7 (2017) 8677–8687.
[44] T. Cordero-Lanzac, R. Palos, J.M. Arandes, P. Castaño, J. Rodríguez-Mirasol, T. Cordero, J. Bilbao, Stability of an acid activated carbon based bifunctional catalyst for the raw bio-oil hydrodeoxygenation, Appl. Catal. B: Environ. 203 (2017) 389–399.
[45] V.O.O. Gonçalves, C. Ciotonea, S. Arrii-Clacens, N. Guignard, C. Roudaut, J. Rousseau, J.M. Clacens, S. Royer, F. Richard, Effect of the support on the hydrodeoxygenation of m-cresol over molybdenum oxide based catalysts, Appl. Catal. B: Environ. 214 (2017) 57–66.
[46] Q. Guan, F. Han, W. Li, Catalytic performance and deoxygenation path of methyl palmitate on Ni_2P/SiO_2 synthesized using the thermal decomposition of nickel hypophosphite, RSC Adv. 6 (2016) 31308–31315.
[47] Q. Guan, F. Wan, F. Han, Z. Liu, W. Li, Hydrodeoxygenation of methyl palmitate over MCM-41 supported nickel phosphide catalysts, Catal. Today 259 (2016) 467–473.
[48] M. Peronia, G. Mancino, E. Baráth, O.Y. Gutiérrez, J.A. Lercher, Bulk and γ-Al_2O_3-supported Ni_2P and MoP for hydrodeoxygenation of palmitic acid, Appl. Catal. B: Environ. 180 (2016) 301–311.
[49] P. Mierczynski, K. Vasilev, A. Mierczynska, W. Maniukiewicz, M.I. Szynkowska, T.P. Maniecki, Bimetallic Au-Cu, Au-Ni catalysts supported on MWCNTs for oxy-steam reforming of methanol, Appl. Catal. B: Environ. 185 (2016) 281–294.
[50] Q. Su, L. Gu, Y. Yao, J. Zhao, W. Ji, W. Ding, C.T. Au, Layered double hydroxides derived $Ni_x(Mg_yAl_zO_n)$ catalysts: enhanced ammonia decomposition by hydrogen spillover effect, Appl. Catal. B: Environ. 201 (2017) 451–460.